Neoplasma 2026; 73(1): 37–51

doi:10.4149/neo_2025_250729N326

Bystin-like protein forms a functional complex with DDX49 to enhance thyroid cancer progression

Yue WANG[1,#], Xiaoxiao XING[1,#], Dongpo ZHANG[1,#], Tao SUN[2,#], Yuren ZHANG[3], Jun LI[1], Daixiang LIAO[1,*], Junyi LI[1,*]

[1]Department of Surgery, Guang'anmen Hospital, China Academy of Chinese Medical Sciences, Beijing, China; [2]Department of Surgery, Guang'anmen Hospital (Baoding), China Academy of Chinese Medical Sciences, Baoding, China; [3]Department of Endocrinology, Guang'anmen Hospital, China Academy of Chinese Medical Sciences, Beijing, China

**Correspondence: 16802002@163.com; bucmljy@163.com*
[#]Contributed equally to this work.

Received July 29, 2025 / Accepted December 8, 2025

The incidence of thyroid cancer is rising worldwide, underscoring the urgent need for novel molecular targets in the management of aggressive disease. This study identifies bystin-like protein (BYSL) as a previously unrecognized oncogenic driver in thyroid carcinoma. Comprehensive analyses of clinical specimens, established cell lines, and patient-derived tumor-like clusters revealed that BYSL is significantly upregulated in thyroid malignancies and is strongly correlated with adverse patient outcomes. Functional assays demonstrated that BYSL promotes tumor cell proliferation, migration, and invasion while suppressing apoptosis. Mechanistically, BYSL interacts directly with DEAD-box helicase 49 (DDX49) to form a functional protein complex that impairs the biogenesis of the tumor suppressor miR-145-5p by inhibiting its DICER-mediated processing. Dual knockdown of BYSL and DDX49 synergistically suppressed tumor growth and induced apoptosis in patient-derived tumor-like cell clusters, with these effects reversed by inhibition of miR-145-5p. Collectively, these findings demonstrate the BYSL-DDX49 complex as a pivotal modulator of thyroid cancer progression and underscore its promise as a therapeutic intervention for restoring tumor-suppressive pathways.

Key words: thyroid carcinoma; BYSL; DDX49; miR-145-5p; protein-protein interaction

Thyroid malignancy constitutes the most prevalent neoplasm among endocrine organs, exhibiting steadily increasing worldwide occurrence over recent decades [1, 2]. Although well-differentiated thyroid neoplasms typically demonstrate favorable clinical outcomes, certain patient populations, especially those harboring aggressive histopathological subtypes, develop disease recurrence, distant spread, and therapeutic resistance to conventional interventions [3, 4]. Existing treatments, including radioiodine and targeted therapies against oncogenic drivers such as BRAF and RET, have improved clinical outcomes, but therapeutic resistance and disease progression remain significant challenges [5, 6]. These challenges underscore the urgent necessity to uncover new molecular determinants and regulatory pathways involved in thyroid tumorigenesis and advancement.

Bystin-like protein (BYSL) is a highly conserved, evolutionarily ancient protein initially recognized for its role in embryo implantation [7]. Subsequent studies have revealed its multifaceted functions in ribosome biogenesis, cell proliferation, adhesion, and signal transduction [8, 9]. Crucially, BYSL is essential for 40S ribosomal subunit assembly and 18S rRNA processing, positioning it at the intersection of cellular growth and metabolic regulation processes frequently altered in cancer [10]. Emerging data suggest that BYSL upregulation functions as a tumorigenic mediator in various cancers, including hepatocellular carcinoma and glioblastoma, facilitating neoplastic cell growth, viability, and metastatic potential through the activation of key molecular pathways, including the AKT/mTOR and GSK-3β/β-catenin networks [9, 11]. Despite these advances, the expression pattern, the roles, molecular activities, and mechanistic contributions of BYSL in thyroid cancer are still not well characterized.

RNA metabolism is a highly orchestrated process integral to cell function and is frequently dysregulated in cancer [12, 13]. DEAD-box (DDX) proteins constitute the most extensive RNA helicase family, participating across nearly all phases of RNA processing, including transcriptional regulation, post-transcriptional modification, nucleocytoplasmic

transport, protein synthesis, and RNA turnover [14–16]. DDX49, a member of this family, exhibits robust ATPase and RNA helicase activities and is essential for mRNA nuclear export, pre-ribosomal RNA processing, and global translational regulation [17]. Upregulation of DDX49 is elevated in multiple malignancies and contributes to tumorigenic characteristics by influencing essential signaling networks [18–20]. However, the functional interplay between BYSL and DDX49 in thyroid cancer has not been investigated.

Protein-protein interactions and the assembly of functional complexes are fundamental to the regulation of RNA metabolism and cellular homeostasis [21, 22]. Such complexes orchestrate a wide range of RNA processing events and can profoundly influence gene expression programs linked to cancer development and progression. Despite growing evidence of their importance, the composition and functional impact of BYSL-containing protein complexes in thyroid cancer remain undefined.

Based on our preliminary data and protein interaction analyses, we hypothesized that BYSL may exert its oncogenic effects in thyroid cancer through the formation of a functional complex with DDX49, thereby modulating key aspects of RNA metabolism and tumor cell behavior. To address this hypothesis, we systematically analyzed BYSL expression profiles and clinical relevance in thyroid cancer, explored its interaction with DDX49, clarified underlying molecular mechanisms, and assessed the biological effects of this protein complex under both cellular and animal model conditions. These results uncover a novel regulatory pathway in thyroid cancer, indicating that BYSL could serve as a potential therapeutic target in this malignancy.

Patients and methods

Tissue specimens and ethical statement. Thyroid malignancy specimens, along with corresponding adjacent normal tissue samples, were collected from 27 patients undergoing thyroidectomy procedures at Guang'anmen Hospital, China Academy of Chinese Medical Sciences. None of the participants had received prior chemotherapy or radiation treatment. Upon surgical removal, tissue samples underwent immediate liquid nitrogen preservation and storage at –80 °C pending RNA extraction. This investigation adhered to the Declaration of Helsinki principles and received institutional approval from the Guang'anmen Hospital Ethics Committee (2022-194-KY-01). Each participant provided written informed consent. Patient clinicopathological data are detailed in Table 1.

Cell culture. Our investigation employed the Nthy-ori 3-1 normal human thyroid epithelial cell line alongside three distinct thyroid malignancy cell lines: TPC-1 (papillary thyroid carcinoma-derived), FTC-133 (follicular thyroid carcinoma-derived), and 8505C (anaplastic thyroid carcinoma-derived). Nthy-ori 3-1 cells were acquired from CRISPRBIO (Beijing, China), while TPC-1, FTC-133, and 8505C cell lines were obtained through the Cell Resource Center at Peking Union Medical College. All cell lines were maintained in RPMI-1640 medium (Sigma-Aldrich, USA) supplemented with 10% fetal bovine serum (FBS), 100 U/ml penicillin, and 100 μg/ml streptomycin. The culture medium for Nthy-ori 3-1 cells was additionally supplemented with 2 mM L-glutamine (Gibco, USA). Cells were incubated at 37 °C in a humidified atmosphere containing 5% CO_2. For routine passage, cells were detached using 0.25% trypsin-EDTA solution (Gibco, USA) when reaching 80–90% confluence, and culture medium was refreshed every 48–72 h.

RNA interference. Short hairpin RNA constructs (shRNAs) directed against human BYSL (sh-BYSL) and DDX49 (sh-DDX49) were synthesized and cloned into the pGPU6/GFP/Neo vector (GenePharma, China), featuring a U6 promoter controlling shRNA transcription and a CMV promoter regulating GFP reporter expression for transfection efficiency assessment. Cellular transfection procedures were conducted at 80% confluence using 2 μg of shRNA plasmid and Lipofectamine™ 2000 (Thermo Fisher Scientific) according to the manufacturer's protocols. Cell collection for subsequent analyses occurred 48–72 h post-transfection. The target sequences of shRNAs are provided in Supplementary Table S1.

For the patient-derived tumor-like cell clusters (PTCs), the same shRNA constructs were packaged into lentiviral particles. The shRNA sequences were inserted into the pLVX-shRNA2 plasmid (Clontech, Mountain View, USA), which contains a CMV promoter driving ZsGreen1 expression for visual monitoring of transduction efficiency. The recombinant constructs were co-delivered with packaging vectors psPAX2 and pMD2.G into HEK293T cells using Lipofectamine™ 2000. Viral particle-containing culture media were collected at 48 and 72 h timepoints post-transfection, subjected to filtration (0.45 μm), and concentrated through ultracentrifugation. PTCs were transduced with lentivirus at an MOI of 20 in the presence of 8 μg/ml polybrene (Sigma-Aldrich). After 48 h, puromycin (2 μg/ml) was applied to select for stably transduced cells.

Plasmid construction and overexpression. Full-length coding sequences of human BYSL and DDX49 underwent PCR amplification and subcloning into the pCMV-Entry vector (OriGene, USA), generating pCMV-BYSL and pCMV-DDX49 constructs, respectively. An empty pCMV-Entry plasmid was used as a negative control. For transient transfection, cells at 80% confluence in 24-well plates were transfected with 2 μg plasmid DNA using Lipofectamine™ 2000 according to the manufacturer's instructions.

For stable overexpression in the microtumor model, the coding sequences of BYSL and DDX49 were subcloned into the pLVX-IRES-Puro lentiviral vector (Clontech, Mountain View, USA). Lentivirus packaging and transduction were performed as described above for shRNA constructs.

microRNA manipulation. Chemically synthesized miR-145-5p mimics (5'-GUCCAGUUUCCCAG-

GAAUCCCUU-3'), antagonists (5'-AGGGAUUCCUG-GGAAAACUGGAC-3'), and corresponding negative controls were purchased from GenePharma (China). For transient delivery, cellular transfection employed 20 nM miRNA mimics or 50 nM antagonists using Lipofectamine™ 2000 (Thermo Fisher Scientific). To establish stable miR-145-5p expression, the miR-145 precursor sequence was cloned into the pCMV-MIR vector (OriGene, USA) and lentiviral production was performed following established protocols. During co-transfection experiments, plasmid delivery preceded miRNA introduction by 6 h. Transfection effectiveness was assessed through qRT-PCR analysis and western blot detection 48–72 hours post-delivery.

RNA extraction and quantitative RT-PCR. Total RNA extraction was performed using the RNeasy Mini Kit for mRNA or the miRNeasy Mini Kit for miRNA (QIAGEN, Germany) according to the manufacturer's protocols. RNA concentration and quality were evaluated using a NanoDrop 2000 spectrophotometer (Thermo Fisher Scientific), with A260/A280 ratios maintained within the 1.8–2.0 range. For mRNA analysis, cDNA synthesis was performed using 1 μg of RNA template with the GoScript Reverse Transcription System (Promega, USA). miRNA and pre-miRNA cDNA preparation utilized the All-in-One miRNA First-Strand cDNA Synthesis Kit (GeneCopoeia, USA). For mature miRNAs and U6 snRNA, real-time PCR was performed using a miRNA-specific forward primer together with the universal reverse primer supplied in the kit. In contrast, pre-miRNAs were amplified using gene-specific forward and reverse primers designed for each target, without the use of the universal reverse primer. Real-time PCR amplification was performed on the ABI PRISM 7300 Real-Time PCR System (Applied Biosystems, USA) using GoTaq qPCR Master Mix (Promega) according to established procedures. Gene expression analysis employed the $2^{-\Delta\Delta Ct}$ calculation method with GAPDH normalization for mRNA or RNU6B for miRNA. Primer details appear in Supplementary Table S2. Experiments were performed in triplicate.

Protein extraction and western blot. Cellular protein isolation employed ProteoJET Mammalian Cell Lysis Reagent (Thermo Fisher Scientific, USA) supplemented with protease and phosphatase inhibitor cocktails (Roche; Sigma-Aldrich), while tissue specimens underwent homogenization in lysis buffer via mechanical homogenizer. Protein quantification was performed using the Pierce BCA Protein Assay Kit (Thermo Fisher Scientific). Equal amounts (50 μg) of protein lysates were separated on 10% SDS-PAGE gels and then electrotransferred onto nitrocellulose membranes (Millipore, USA). Following 5% non-fat milk/TBST blocking, membranes were incubated overnight at 4 °C with primary antibodies: anti-BYSL (#ab251811, 1:1000, Abcam, USA), anti-DDX49 (#sc-514928, 1:1000, Santa Cruz Biotechnology, USA), and anti-GAPDH (#5174, 1:1000, Cell Signaling Technology, USA). Subsequently, membranes were incubated at room temperature for 1 h with HRP-conjugated secondary antibodies (Cell Signaling Technology, 1:5000) after appropriate washing steps. Protein detection utilized SuperSignal West Pico PLUS substrate (Thermo Fisher Scientific) with signal capture via ChemiDoc MP Imaging System (Bio-Rad, USA). Band intensity analysis was employed using ImageJ software with GAPDH normalization.

Immunoprecipitation (co-IP). Cellular protein lysates underwent preparation in IP lysis buffer (25 mM Tris-HCl, pH 7.4, 150 mM NaCl, 1% NP-40, 1 mM EDTA, 5% glycerol) supplemented with protease inhibitor cocktail (Roche). Each co-IP experiment utilized 500 μg of total protein combined with 2 μg of specific antibodies: anti-BYSL (#sc-271722, Santa Cruz Biotechnology), anti-DDX49 (#sc-514928, Santa Cruz Biotechnology), or control IgG, followed by overnight incubation at 4 °C with gentle agitation. Protein A/G magnetic beads (25 μl, Thermo Fisher Scientific) were subsequently added, followed by a 2 h incubation at 4 °C. Immunocom-

Table 1. Clinicopathological characteristics of thyroid cancer patients.

Characteristics	n (%) or mean ± SD
Total patients	27
Gender	
Male	6 (22.2)
Female	21 (77.8)
Age (years)	46.2 ± 12.8
> 45	14 (51.9)
≤ 45	13 (48.1)
Tumor size (cm)	2.8 ± 1.4
> 2	16 (59.3)
≤ 2	11 (40.7)
Histological type	
Papillary thyroid carcinoma	20 (74.1)
Follicular thyroid carcinoma	5 (18.5)
Anaplastic thyroid carcinoma	2 (7.4)
Clinical stage (AJCC 8th edition)	
I	12 (44.4)
II	7 (25.9)
III	5 (18.5)
IV	3 (11.2)
I+II	19 (70.4)
III+IV	8 (29.6)
Lymph node metastasis	
Positive (N1)	10 (37.0)
Negative (N0)	17 (63.0)
Extrathyroidal extension	
Present	9 (33.3)
Absent	18 (66.7)
Vascular invasion	
Present	7 (25.9)
Absent	20 (74.1)
Multifocality	
Present	8 (29.6)
Absent	19 (70.4)

plexes received magnetic separation and quadruple washing with IP wash buffer (25 mM Tris-HCl, pH 7.4, 150 mM NaCl, 0.1% NP-40). Protein elution occurred after 5 minutes of boiling in 2× Laemmli buffer at 95 °C. Recovered immunoprecipitates were subjected to western blot analysis using the specified antibodies. For the western blot, 10% of the total lysate was loaded as input, and the entire IP eluate was loaded for detection. Exposure times were optimized for sensitivity. Accordingly, IP and input band intensities are not directly comparable, and the co-IP assays were intended as qualitative evidence of interaction rather than an estimate of the bound/unbound fractions.

Immunofluorescence co-localization. Coverslip-cultured cells underwent fixation in 4% paraformaldehyde for 15 min at ambient temperature, followed by permeabilization using 0.1% Triton X-100 for 10 min. After 1 h of blocking in 3% BSA, cells were incubated overnight at 4 °C with primary antibodies: anti-BYSL (1:200, #ab251811, Abcam) and anti-DDX49 (1:200, #sc-514928, Santa Cruz Biotechnology). Subsequently, cells were washed with PBS and incubated for 1 h at room temperature in the dark with Alexa Fluor 488-conjugated anti-rabbit and Alexa Fluor 594-conjugated anti-mouse secondary antibodies (1:500, Invitrogen). Nuclear counterstaining employed DAPI (1:1000, Sigma-Aldrich) for 5 minutes. Image acquisition was performed using an Olympus IX71 inverted fluorescence microscope. Co-localization analysis proceeded via ImageJ.

Database analysis and bioinformatics. Public tumor-normal expression comparisons were performed using the Assistant for Clinical Bioinformatics (ACLBI) platform, which includes TCGA-THCA tumors (T=512) and an expanded pool of normal thyroid tissues (N=712). miR-145-5p expression data were obtained from ENCORI/starBase [23]. Survival analyses were performed using Kaplan-Meier methods with median expression cutoffs obtained from GEPIA3 [24]. Protein-protein association networks were predicted using STRING (version 12.0) with a required score set to high confidence (>0.700) [25]. Molecular docking studies between BYSL and DDX49 were performed using the ZDOCK algorithm, which utilized crystallographic data from the PDB database. Statistical correlation was analyzed using Pearson's coefficient methodology with a significance threshold of $p<0.05$.

RNA immunoprecipitation (RIP). Cell harvesting proceeded with RIP buffer lysis (20 mM Tris-HCl, pH 7.5, 150 mM NaCl, 1 mM EDTA, 0.5% NP-40) containing RNase inhibitor (Thermo Fisher Scientific) and protease inhibitor cocktail. Cellular lysates (500 μg) were treated overnight at 4 °C with 5 μg target antibodies: anti-DDX49 (#sc-271722, Santa Cruz Biotechnology), anti-BYSL (#sc-514928, Santa Cruz Biotechnology), anti-Dicer (#5362, Cell Signaling Technology), or control IgG. Protein A/G magnetic beads (50 μl) underwent subsequent addition with 2 h 4 °C incubation. After six consecutive RIP buffer washes, RNA-protein-antibody immunocomplexes underwent RNA isolation via TRIzol methodology (Invitrogen) following standard protocols. Recovered RNA received reverse transcription processing and qRT-PCR analysis as described earlier. Target RNA enrichment calculation employed fold-change comparison to IgG control, using 1% input sample for normalization purposes.

Cell proliferation assay. Cell proliferation was assessed using the Cell Counting Kit-8 (CCK-8) assay (Dojindo, Japan). Cell suspensions (3×10^3 cells/well) were seeded in 96-well plates with culture maintenance at designated time intervals. At each experimental time point, 10 μl CCK-8 reagent was added to individual wells, followed by 2 h incubation at 37 °C. Absorbance detection occurred at 450 nm using a microplate spectrophotometer. Growth kinetics derived from mean absorbance values of triplicate determinations.

Migration and invasion assays. Cell migration and invasion capabilities were evaluated using Transwell chamber assays (8 μm pore diameter, Corning). Migration studies involved 5×10^4 cells in serum-free medium within the upper chambers. For invasion assessment, chamber membranes were coated with Matrigel (BD Biosciences) at a 1:8 dilution under serum-free conditions. Complete medium containing 10% FBS functioned as a chemoattractant in the lower chambers. After 24 hours of culture, non-migrated cells were removed with a cotton swab, while the transferred cell populations were fixed with 4% paraformaldehyde and stained with 0.1% crystal violet. Microscopic analysis captured five random fields per chamber at 200× magnification, with cell counting performed via ImageJ software.

Apoptosis analysis. Apoptotic cell death was assessed using the Annexin V-FITC/PI Detection Kit (BD Biosciences). After trypsinization, the cells were washed twice with PBS and resuspended in 1× binding buffer at a concentration of 1×10^6 cells/ml. Cell suspension aliquots (100 μl) were treated with 5 μl Annexin V-FITC and 5 μl propidium iodide, followed by 15 min dark incubation at room temperature. Subsequently, 400 μl binding buffer addition preceded flow cytometric detection (BD FACSCalibur). Early and late apoptotic cells were defined as Annexin V^+/PI^- and Annexin V^+/PI^+, respectively, with viable cells as Annexin V^-/PI^-. Total apoptosis was calculated as the sum of early and late apoptotic populations and reported as a percentage of the total cell population. A minimum of 10,000 events was acquired for each sample, and data analysis was performed using FlowJo software version 10.8 (BD Biosciences).

Mouse xenograft model. *In vivo* studies received institutional approval from the Guang'anmen Hospital Ethics Board (VS2126A00172). Six-week-old female NOD-SCID mice (VIEWSOLID BIOTECH, China) were maintained in standard specific pathogen-free facilities. 8505C cells bearing stable transfections (sh-NC, sh-BYSL, or pCMV-BYSL constructs) were collected and prepared at a 4×10^7 cells/ml concentration in serum-depleted media. Animals were randomly assigned into three cohorts (n=5 per cohort) and received subcutaneous implantation of a 100 μl cellular

suspension (4×10^6 cells) at the right dorsal flank under isoflurane anesthesia.

Tumor dimensions were monitored every 3 days using digital calipers with volume calculations following the formula: $V=(\text{length}\times\text{width}^2)/2$. At 4 weeks post-implantation, animals were euthanized, and neoplasms were harvested, weighed, and prepared for histopathological examination (10% formalin preservation) and molecular investigations (liquid nitrogen snap-freezing).

Patient-derived tumor-like cell clusters (PTCs) model. Primary thyroid malignancy specimens underwent processing according to the methodology established by Yin et al. [26]. Fresh tissue was enzymatically disaggregated via collagenase treatment, then filtered and cultured in suspension vessels with enriched Advanced DMEM medium containing essential growth supplements. The complete composition and reagent sources are provided in Supplementary Table S3. PTCs received lentiviral transduction with vectors carrying sh-NC, sh-BYSL, sh-DDX49, or dual sh-BYSL+sh-DDX49 constructs. For rescue experiments, the miR-145-5p inhibitor or a matched negative control was introduced into sh-BYSL+sh-DDX49-modified PTCs. Growth capacity was monitored through microscopic observation, while cell viability was assessed via the CellTiter-Glo assay. Morphological changes underwent characterization through immunohistochemical analysis and molecular evaluation of key biomarkers.

Histological analysis. Thyroid tumor patient samples or PTCs were fixed in 10% neutral buffered formalin for 24 h, then paraffin-embedded and 4 μm sectioned. Hematoxylin-eosin staining was performed following standard protocols. For immunohistochemical assessment, tissue sections underwent deparaffinization, rehydration, and antigen retrieval using citrate buffer (pH 6.0) at 95 °C for 15 min. Endogenous peroxidase neutralization employed 3% hydrogen peroxide treatment. Sections received primary antibody exposure targeting Ki-67 (1:200), BYSL (1:200, #ab251811, Abcam), or DDX49 (1:100, #514928, Santa Cruz Biotechnology) via overnight 4 °C incubation, followed by HRP-conjugated secondary antibody treatment for 1 h at room temperature. DAB functioned as a chromogenic developer with hematoxylin nuclear counterstain. Microscopic imaging was performed using the Olympus BX53 system at 200× magnification. Five random fields per section received ImageJ software analysis. Ki-67 and cleaved-Caspase-3 positive cells were calculated as percentages of the total cell population through counting a minimum of 500 cells per sample.

ATP activity assay. Cellular ATP content was determined using the CellTiter-Glo 3D Cell Viability assay (Promega, USA), which operates on the principle that ATP quantification correlates with metabolically viable cells via luciferase-mediated bioluminescent detection. Thyroid malignancy cells or PTCs were plated in 96-well opaque microplates (1×10^4 cells/well or 30–50 PTCs/well). Following experimental treatments, microplates underwent room temperature equilibration for 30 min, after which 100 μl CellTiter-Glo solution was dispensed to individual wells containing equivalent culture medium volumes. Plate contents were agitated on the orbital platform for 5 min to facilitate cellular lysis, then incubated for 25 min at ambient temperature to achieve luminescent signal stabilization. Bioluminescence detection was performed using the Synergy microplate detection system (BioTek, USA) with 0.5–1 second integration intervals per well. ATP concentrations were standardized against control cohorts and expressed as relative luminescence units (RLU) or control percentages. Each assay was conducted in triplicate with three independent repetitions.

Flow cytometry of Ki-67 and cleaved caspase-3 in PTCs. PTCs were gently dissociated to single cells with Accutase (Sigma-Aldrich) for 10–15 min at 37 °C, passed through a 40 μm strainer, fixed with 4% paraformaldehyde (10 min, RT), and permeabilized with 0.1% Triton X-100 (10 min). Cells were incubated with rabbit anti-Ki-67 (1:200, #9129, Cell Signaling Technology) or rabbit anti-cleaved caspase-3 (Asp175) (1:100, #9664, Cell Signaling Technology), followed by Alexa Fluor 488-conjugated goat anti-rabbit IgG secondary antibody (1:500, Invitrogen). Matched rabbit IgG isotype controls (#3900, Cell Signaling Technology) and unstained controls were processed in parallel. Data were acquired on a BD FACSCanto II (488 nm laser; FITC 530/30) with constant PMT voltages across groups within each staining batch and analyzed in FlowJo v10.8 (BD). The detailed flow-cytometric gating strategy, including debris and singlet exclusion and isotype-based positivity thresholds for Ki-67 and cleaved caspase-3, is provided in the Supplementary information and illustrated in Supplementary Figure S1.

Statistical analysis. Statistical evaluation was performed using GraphPad Prism 9.0 software (GraphPad Software, USA). Data presentation utilized mean ± standard deviation (SD) from a minimum of three independent experiments. Two-group comparisons received a two-tailed Student's t-test analysis. Multiple group assessments employed one-way ANOVA followed by Tukey's post hoc comparison. Dual-variable experiments underwent two-way ANOVA evaluation. Pearson's correlation coefficient determined associations between continuous variables. Statistical significance threshold was set at $p<0.05$ (*$p<0.05$, **$p<0.01$, ***$p<0.001$). Survival analysis was performed using Kaplan-Meier curves with a log-rank test for comparison. Data visualization employed GraphPad Prism 9.0, with error bars representing SD and sample sizes specified in Figure Legends.

Results

BYSL is overexpressed in thyroid cancer and correlates with poor prognosis. To comprehensively evaluate BYSL expression profiles in thyroid neoplasms, we first analyzed BYSL transcript levels in thyroid carcinoma (THCA) samples from The Cancer Genome Atlas (TCGA) database and normal thyroid tissues from the GTEx repository. Using

the ACLBI platform (https://www.aclbi.com/static/index.html), BYSL expression was significantly higher in tumors than in normal thyroid tissues (Figure 1A), with x-axis labels indicating sample sizes (Tumor, n=512; Normal, n=712).

To confirm these findings, qRT-PCR assessment was performed on tumor and adjacent normal tissues from 27 thyroid cancer patients. Consistent with bioinformatics data, BYSL mRNA levels were markedly increased in tumor tissues versus paired normal tissues (Figure 1B, p<0.001). Western blot analysis further confirmed elevated BYSL protein levels in thyroid cancer tissues compared to normal tissues (Figure 1C).

At the cellular level, BYSL expression was assessed in the normal thyroid follicular cell line Nthy-ori 3-1 and various thyroid cancer cell lines (TPC-1, FTC-133, 8505C) using qRT-PCR and western blot techniques. Both mRNA and protein expression of BYSL demonstrated a substantial increase in all thyroid cancer cell lines relative to Nthy-ori 3-1 (Figures 1D, 1E), supporting BYSL overexpression in thyroid carcinogenesis.

To assess the clinical relevance of BYSL, we examined its association with patient prognosis and clinicopathological variables in the TCGA-THCA dataset. Using GEPIA3 with a prespecified median split, BYSL expression was not signifi-

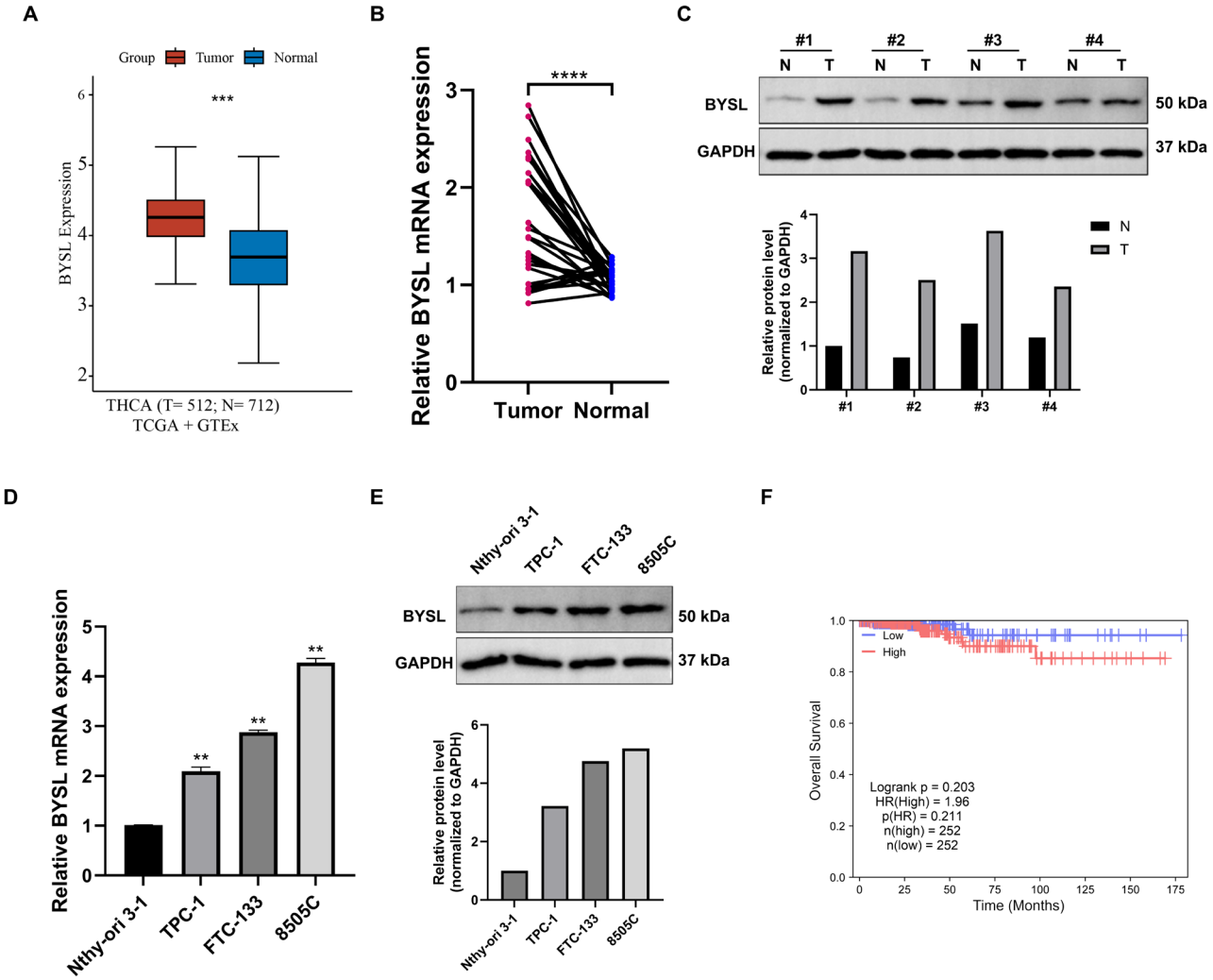

Figure 1. Analysis of BYSL expression in thyroid cancer tissues, cell lines, and its association with clinical outcome. A) Boxplot of BYSL expression in TCGA-THCA tumors versus normal thyroid tissues derived from the ACLBI platform. Sample sizes are indicated on the x-axis: Tumor (n=512) and Normal (n=712). ***p<0.001; B) Quantitative real-time PCR analysis of BYSL mRNA expression in paired tumor and adjacent normal thyroid tissues from 27 thyroid cancer patients. Statistical significance determined by paired t-test, ****p<0.0001; C) Western blot analysis of BYSL protein levels in four pairs of thyroid carcinomas (T) and adjacent normal (N) tissues. GAPDH served as a loading control. Densitometric quantification normalized to GAPDH is shown below; D) Relative BYSL mRNA expression measured by qRT-PCR in normal thyroid follicular epithelial cells (Nthy-ori 3-1) and thyroid cancer cell lines (TPC-1, FTC-133, 8505C). Data represent mean ± SD, n=3. **p<0.01 vs. Nthy-ori 3-1 (one-way ANOVA with Tukey's post hoc test); E) Western blot analysis and densitometric quantification of BYSL protein levels in Nthy-ori 3-1 and thyroid cancer cell lines. GAPDH served as a loading control; F) Kaplan-Meier OS analysis for BYSL in TCGA-THCA generated using GEPIA3 with the default median split (Low, n=252; High, n=252). Median OS was not reached in either group. Two-sided log-rank p=0.203; Cox HR=1.96 (95% CI 0.68-5.66), p=0.211.

cantly associated with overall survival (OS) (Figure 1F). Median OS was not reached in either group, consistent with the low event rate in THCA. Similarly, no significant associations were observed between BYSL expression and tumor size, clinical stage, or lymph-node status.

BYSL promotes proliferation, migration, and invasion while suppressing apoptosis in thyroid cancer cells. To elucidate BYSL functional roles in thyroid cancer, we conducted loss- and gain-of-function experiments in thyroid cancer cell lines using siRNA-mediated knockdown and plasmid-mediated overexpression, respectively. Successful BYSL expression manipulation was confirmed through qRT-PCR and western blot analysis (Figures 2A, 2B).

CCK-8 proliferation experiments showed that BYSL knockdown significantly reduced cell proliferation in thyroid cancer cells (TPC-1 and 8505C), while BYSL overexpression enhanced cellular growth (Figure 2C). Transwell migration and invasion assays revealed that BYSL silencing markedly decreased, whereas overexpression increased, the migratory and invasive capabilities of thyroid cancer cells (Figures 2D, 2E), indicating BYSL participation in promoting tumor cell motility and invasion.

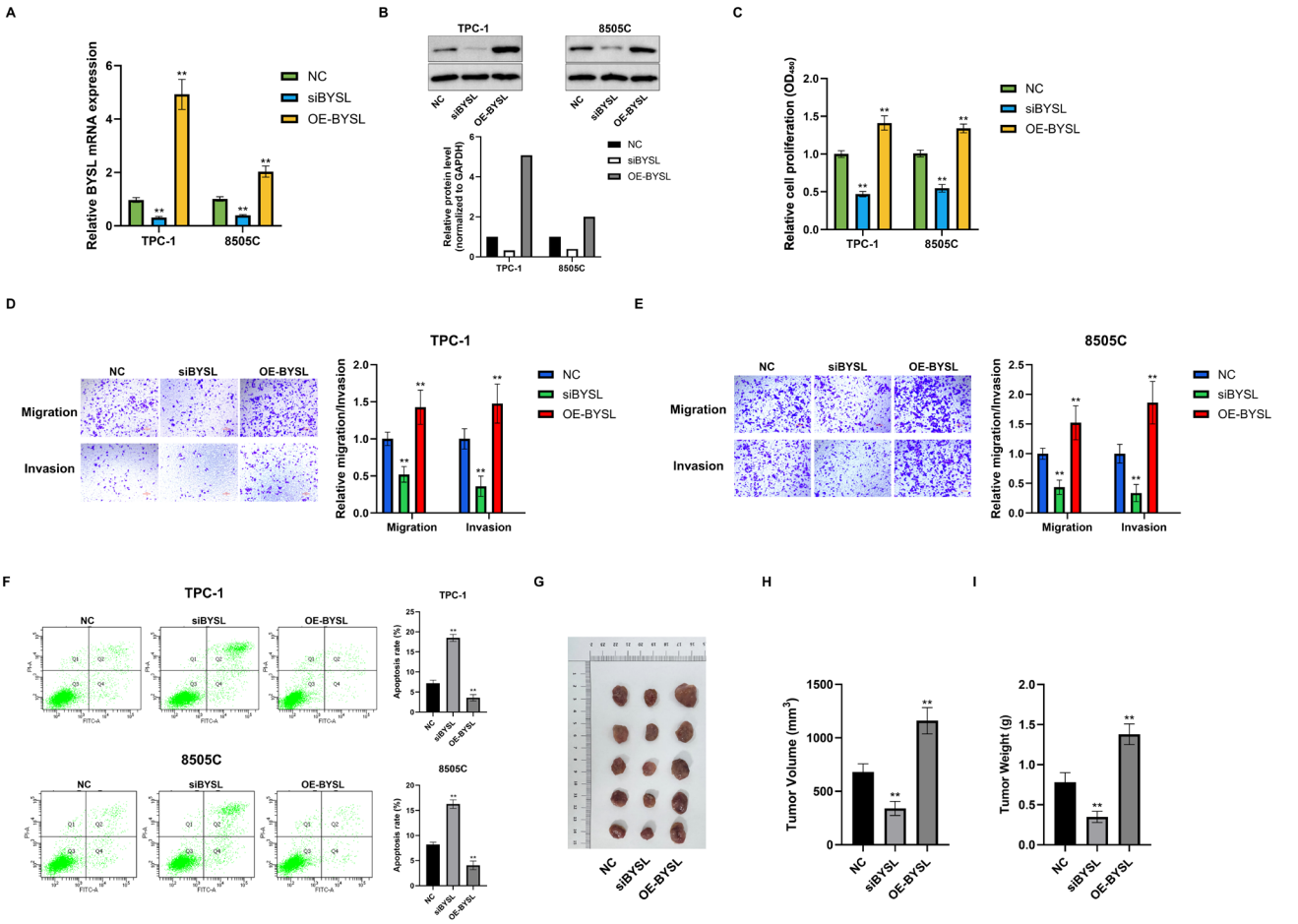

Figure 2. Effects of BYSL knockdown and overexpression on thyroid cancer cell proliferation, migration, invasion, apoptosis, and tumor growth. A) Relative BYSL mRNA expression in TPC-1 and 8505C cells following siRNA-mediated knockdown (siBYSL), plasmid-mediated overexpression (OE-BYSL), or negative control (NC), measured by qRT-PCR. Data represent mean ± SD, n=3. **p<0.01 vs. NC (one-way ANOVA with Tukey's post hoc test); B) Western blot analysis and densitometric quantification of BYSL protein levels in TPC-1 and 8505C cells under the indicated conditions. GAPDH was used as a loading control; C) CCK-8 assay of cell proliferation in TPC-1 and 8505C cells with the indicated treatments. Data represent mean ± SD, n=3. **p<0.01 vs. NC; D, E) Representative images (top) and quantification (bottom) of Transwell migration and invasion assays in TPC-1 (D) and 8505C (E) cells after the indicated treatments. Data represent mean ± SD, n=3. **p<0.01 vs. NC; F) Flow cytometric analysis and quantification of apoptosis in TPC-1 and 8505C cells after the indicated treatments. Apoptotic cells were identified by Annexin V-FITC/PI dual staining, with early apoptotic cells defined as Annexin V^+/PI^- and late apoptotic cells as Annexin V^+/PI^+. Representative flow cytometry plots (left panels) and quantification (right bar graphs) are shown. All apoptosis percentages, including control (NC) values, represent experimentally measured data from three independent experiments. Data represent mean ± SD, n=3. **p<0.01 vs. NC (one-way ANOVA with Tukey's post hoc test); G) Representative images of subcutaneous xenograft tumors formed by TPC-1 cells with the indicated treatments in nude mice; H, I) Quantification of tumor volume (H) and tumor weight (I) in xenograft models. Data represent mean ± SD, n=5/group. **p<0.01 vs. NC. Abbreviations: NC-negative control; siBYSL-BYSL knockdown; OE-BYSL-BYSL overexpression.

Flow cytometry analysis revealed that BYSL knockdown significantly increased apoptosis rates in thyroid cancer cells, while BYSL overexpression exhibited anti-apoptotic effects (Figure 2F). The baseline apoptosis observed in negative control (NC) samples represents the intrinsic background apoptosis under standard culture conditions and was reproducibly measured across independent biological replicates. These findings collectively suggest that BYSL not only promotes proliferation and invasion but also suppresses programmed cell death in thyroid cancer cells.

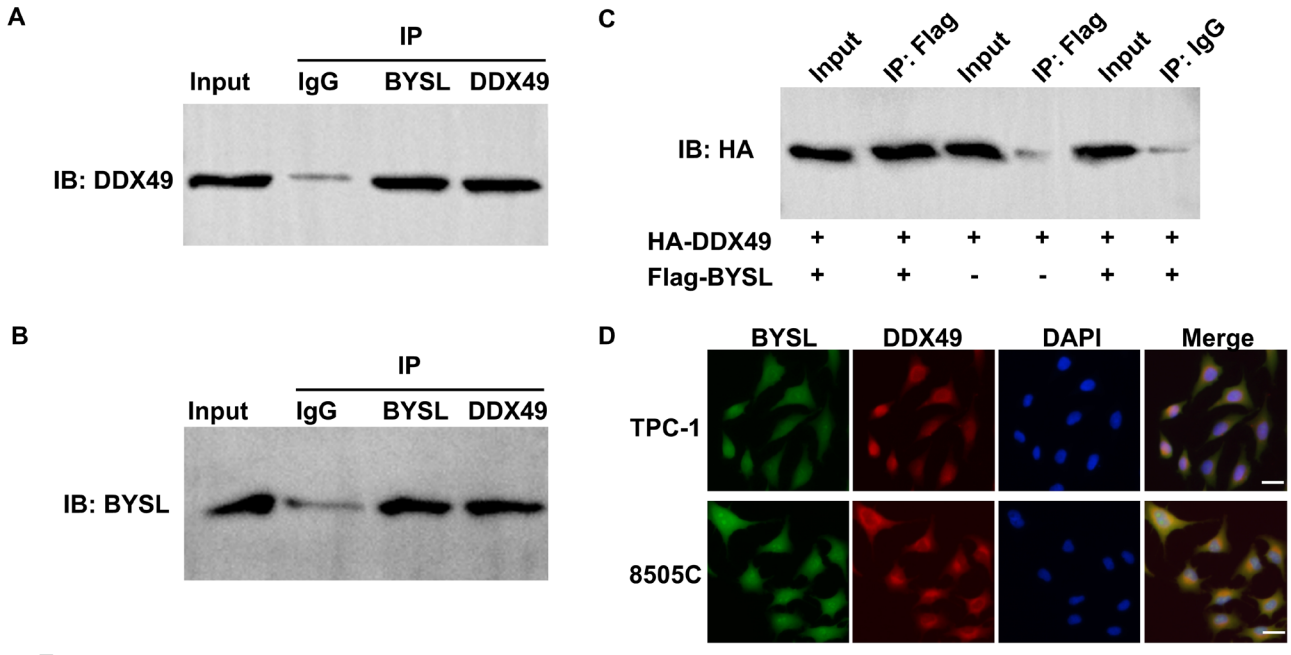

E

#node1	node2	node1_string_id	node2_string_id	coexpression	experimentally_determined_interaction	automated_text mining	combined_score
BYSL	DDX49	9606.ENSP00000230340	9606.ENSP00000247003	0.752	0.477	0.822	0.975

F

Rank	1
Docking Score	-226.72
Confidence Score	0.8226
Ligand rmsd (Å)	81.33
Interface residues	model_1

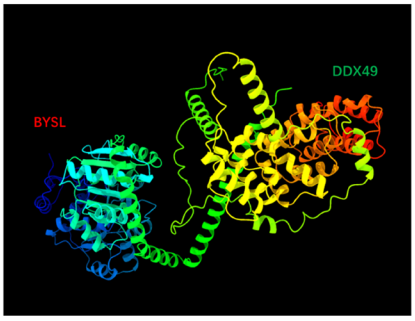

Figure 3. Analysis of the interaction between BYSL and DDX49 in thyroid cancer cells. A) Co-immunoprecipitation (co-IP) of endogenous BYSL from thyroid cancer cell lysates, followed by immunoblotting (IB) for DDX49; B) Reciprocal co-IP of endogenous DDX49 from thyroid cancer cell lysates, followed by immunoblotting for BYSL; C) co-IP analysis in cells co-transfected with Flag-tagged BYSL and HA-tagged DDX49. Cell lysates were immunoprecipitated (IP) with anti-Flag antibody or IgG control and immunoblotted with anti-HA antibody. Note: co-IP assays in (A-C) are qualitative; inputs and IPs were loaded at different proportions and imaged under different exposures. Serial (repeat) immunoprecipitation was not performed, and band intensities should not be used to infer that all BYSL or DDX49 is in complex; D) Immunofluorescence staining showing subcellular localization of BYSL (green) and DDX49 (red) in TPC-1 and 8505C cells. Nuclei are stained with DAPI (blue). Scale bars, 20 μm; E) STRING database analysis of predicted interaction between BYSL and DDX49, including combined interaction score; F) Structural modeling and molecular docking results for BYSL and DDX49, showing docking score, confidence score, ligand rmsd, and interface residues.

To assess *in vivo* relevance, we established subcutaneous xenograft models in immunodeficient mice. Tumors derived from BYSL-knockdown cells exhibited significantly reduced growth rates, tumor sizes, and weights compared to those of the controls (Figures 2G–2I). In contrast, BYSL overexpression promoted xenograft growth and increased tumor burden. Together, these *in vitro* and *in vivo* results confirm a crucial oncogenic role for BYSL in thyroid cancer progression.

BYSL directly interacts with DDX49 to form a functional protein complex. To decipher the molecular mechanisms underlying BYSL function, we focused on its potential interaction with DDX49. Co-IP assays demonstrated that endogenous BYSL forms a complex with DDX49 in thyroid cancer cells (Figure 3A). Reciprocal co-IP further confirmed this direct protein-protein interaction (Figure 3B). These co-IP experiments were qualitative and not designed to quantify the proportion of BYSL or DDX49 residing in the complex; we did not conduct sequential immunoprecipitation to assess depletion of the partner pool.

Using overexpression systems for Flag-tagged BYSL and HA-tagged DDX49, we observed specific co-precipitation of the two proteins, which was absent in control groups (Figure 3C), further substantiating their direct interaction. Immunofluorescence co-localization experiments revealed prominent co-localization of BYSL and DDX49 in both nucleoli and cytoplasm (Figure 3D), indicating potential subcellular cooperation.

Bioinformatic analyses using STRING and structural docking further supported a high interaction score and the likelihood of stable complex formation between BYSL and DDX49 via defined domains (Figures 3E, 3F). Together, these results provide compelling evidence that BYSL and DDX49 directly interact to form a functional complex in thyroid cancer cells.

The BYSL-DDX49 complex exhibits an inverse relationship with miR-145-5p. In this study, we did not aim to perform an exhaustive, unbiased screen of all deregulated miRNAs; instead, we a priori focused on miR-145-5p because it is a well-established tumor-suppressive miRNA in

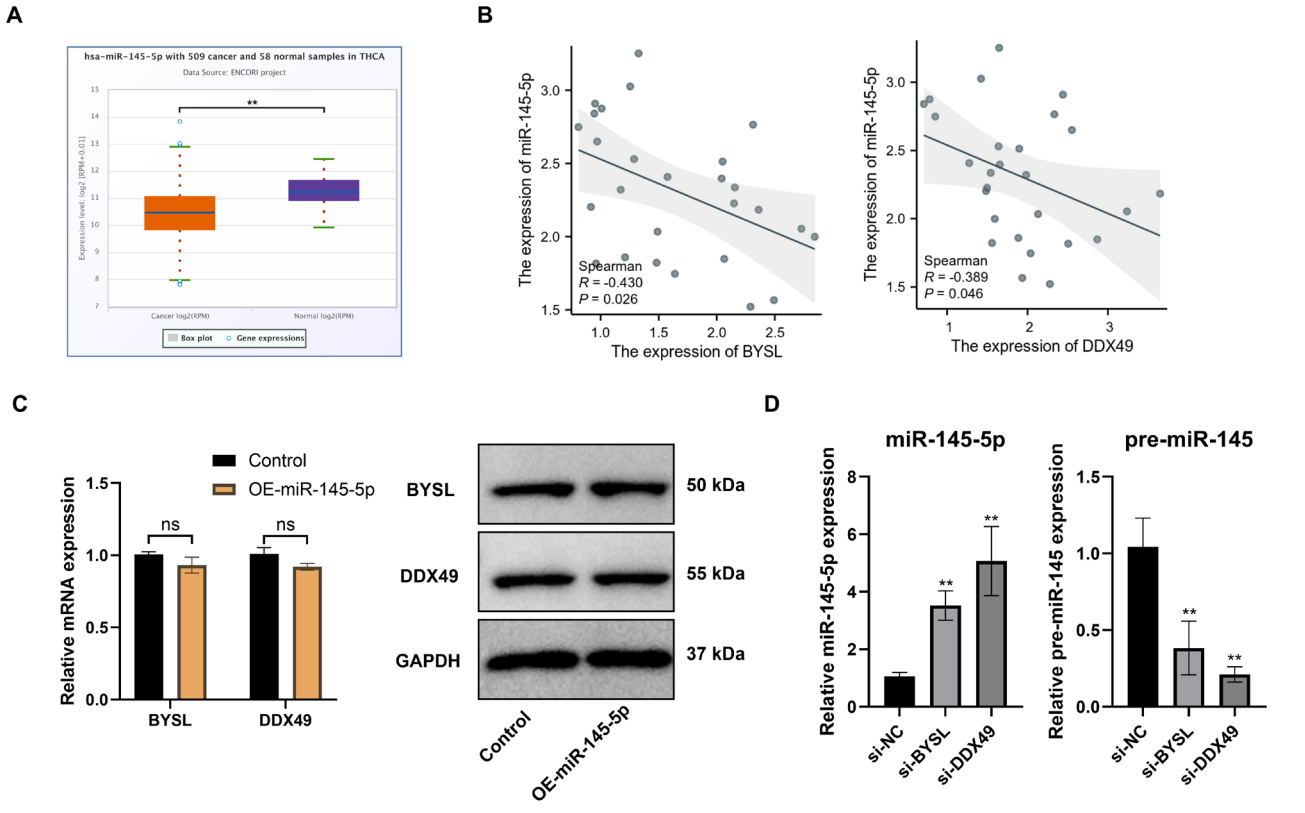

Figure 4. Analysis of miR-145-5p expression and its association with BYSL and DDX49 in thyroid cancer. A) Boxplot showing the expression levels of miR-145-5p in thyroid carcinoma (THCA, n=509) and normal thyroid tissues (n=58) from the starBase database. Statistical significance determined by t-test, **p<0.01; B) Scatter plots showing Spearman correlations between miR-145-5p and BYSL (left) or DDX49 (right) derived from our institutional cohort of primary THCA specimens (n=27). Correlation coefficients (ρ) and p-values are indicated; C) Quantitative RT-PCR (left) and western blot analysis (right) of BYSL and DDX49 expression following overexpression of miR-145-5p (OE-miR-145-5p) or control in thyroid cancer cells. Abbreviations: ns-not significant; D) Quantitative RT-PCR analysis of mature miR-145-5p (left) and pre-miR-145 (right) levels in thyroid cancer cells transfected with siRNAs targeting BYSL (si-BYSL), DDX49 (si-DDX49), or negative control (si-NC). Data represent mean ± SD, n=3. Statistical significance determined by one-way ANOVA with Tukey's post hoc test, **p<0.01 vs. si-NC.

thyroid carcinoma [27–29] and thus a biologically plausible candidate downstream of BYSL-DDX49. To investigate the molecular mechanisms by which the BYSL-DDX49 complex facilitates thyroid malignancy progression, we first examined public miRNA expression profiles for THCA using the ENCORI/starBase (TCGA-THCA) dataset and confirmed that miR-145-5p is significantly downregulated in tumors compared to normal thyroid tissue ($p<0.01$; Figure 4A). In our institutional cohort comprising 27 primary THCA specimens, miR-145-5p levels inversely correlated with BYSL and with DDX49 (Spearman $r=-0.430$, $p=0.026$; and $r=-0.389$, $p=0.046$, respectively), as shown in Figure 4B, further supporting miR-145-5p as a clinically relevant readout of BYSL-DDX49 activity in this setting.

At the cellular level, miR-145-5p overexpression failed to modify the transcript or protein abundance of BYSL or DDX49 (Figure 4C), indicating that the inverse correlation does not result from direct miR-145-5p-mediated regulation. Nevertheless, silencing of either BYSL or DDX49 in thyroid malignant cells substantially elevated mature miR-145-5p while reducing pre-miR-145 abundance (Figure 4D), suggesting that BYSL and DDX49 may regulate miR-145-5p maturation through interference with pre-miR-145 processing mechanisms.

The BYSL-DDX49 complex cooperatively binds pre-miR-145. To further explore the mechanism through which the BYSL-DDX49 complex regulates miR-145 biogenesis, we conducted RNA immunoprecipitation (RIP) experiments. Both BYSL and DDX49 demonstrated binding to pre-miR-145, with co-expression markedly increasing binding affinity (Figure 5A).

Remarkably, DDX49 silencing nearly eliminated the interaction between BYSL and pre-miR-145, while BYSL silencing significantly decreased DDX49's binding to pre-miR-145 (Figure 5B). Western blot examination verified that silencing of BYSL or DDX49 did not influence the protein expression of each other (Figure 5C), suggesting that the observed effects result from functional interaction rather than changed protein levels.

To evaluate the binding specificity of the BYSL-DDX49 complex, we conducted RIP experiments using multiple control pre-miRNAs, including pre-miR-21, pre-Let-7a, and pre-miR-200c. In contrast to pre-miR-145, these control pre-miRNAs exhibited minimal enrichment with BYSL or DDX49 antibodies (Figure 5D), demonstrating the specificity of BYSL-DDX49 complex binding to pre-miR-145.

These findings indicate that BYSL's interaction with pre-miR-145 requires DDX49, and that BYSL promotes DDX49's binding to pre-miR-145. Therefore, the BYSL-DDX49 complex probably functions collaboratively in pre-miR-145 processing, although the detailed mechanisms require additional investigation.

BYSL-DDX49 complex regulates DICER-mediated pre-miR-145 processing and tumor cell phenotypes. To clarify the molecular mechanisms by which the BYSL-DDX49 complex modulates miR-145 maturation, we investigated DICER and pre-miR-145 interactions under various experimental conditions. Co-IP analyses demonstrated that BYSL-DDX49 complex upregulation reduced DICER-pre-miR-145 association (Figure 6A), while BYSL or DDX49 silencing enhanced this interaction (Figure 6B). In conjunction with RIP experimental data, these observations indicate that the BYSL-DDX49 complex may competitively sequester pre-miR-145, consequently disrupting DICER-mediated miRNA processing and restricting miR-145-5p maturation.

From a functional perspective, BYSL upregulation substantially enhanced proliferative capacity, migratory behavior, and invasive potential of thyroid malignancy cells (Figures 6C, 6D). Importantly, DDX49 silencing or miR-145-5p restoration through mimic transfection partially counteracted the oncogenic characteristics induced by BYSL upregulation (Figures 6C, 6D), demonstrating that miR-145-5p functions as a critical downstream mediator of the BYSL-DDX49 regulatory pathway in facilitating thyroid malignancy progression.

PTCs validate the functional and mechanistic significance of the BYSL-DDX49-miR-145-5p axis. For enhanced recapitulation of tumor microenvironmental conditions and validation of clinical significance for the BYSL-DDX49 complex, we generated PTC models from primary thyroid malignancy specimens. Immunohistochemical analysis revealed that BYSL and DDX49 expression profiles in PTCs closely replicated those detected in primary neoplasms (Figure 7A). For functional evaluation, PTCs were allocated to four experimental cohorts: sh-NC (control), sh-BYSL, sh-DDX49, and sh-BYSL+sh-DDX49 (combined silencing).

Both individual and combined silencing of BYSL or DDX49 substantially impaired PTCs development, with the combined silencing cohort demonstrating the most pronounced antitumor effects (Figure 7B). Intracellular flow cytometry of cleaved caspase-3 revealed increased apoptotic fractions across all treatment groups, with the highest cleaved caspase-3-positive percentage in the combined sh-BYSL+sh-DDX49 group. qRT-PCR evaluation confirmed that BYSL and/or DDX49 inhibition resulted in substantial miR-145-5p upregulation, most prominently in the combined silencing cohort (Figure 7D). Flow cytometric analysis of Ki-67 revealed diminished proliferative fractions in both single-gene silencing groups, with the lowest Ki-67 positivity under combined silencing (Figure 7E).

For additional validation of miR-145-5p's essential function in mediating BYSL/DDX49-driven tumor suppression, rescue studies were conducted using miR-145-5p antagonists in BYSL or DDX49 silencing contexts. miR-145-5p inhibitor administration effectively counteracted the suppressive effects on microtumor development induced by BYSL or DDX49 silencing, as demonstrated by enhanced ATP activity (Figure 7F), elevated Ki-67 positivity (Figure 7G), and diminished cleaved caspase-3-positive cellular fractions (Figure 7H), restoring tumor cellular characteristics to near-

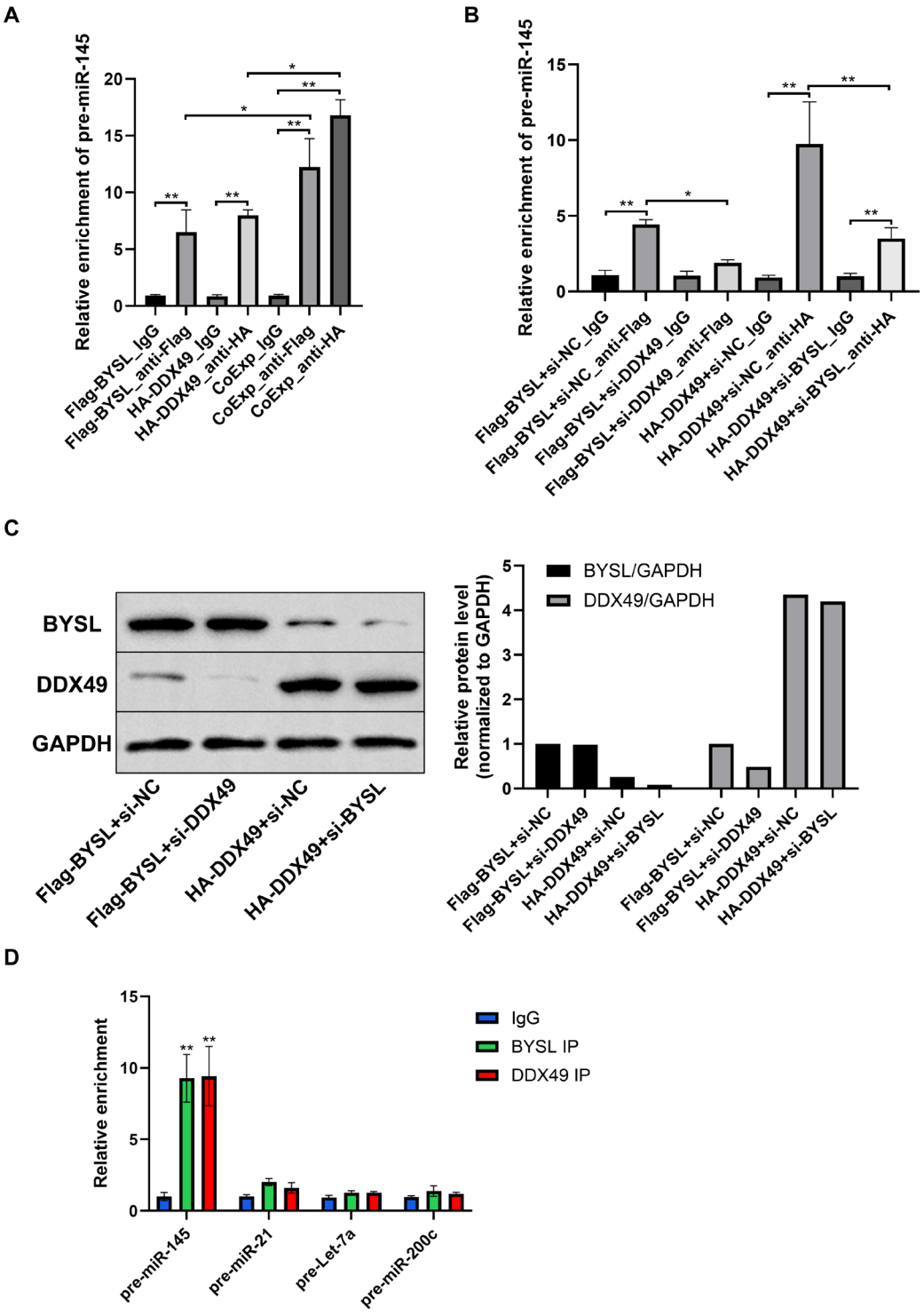

Figure 5. RNA immunoprecipitation (RIP) reveals cooperative binding of BYSL and DDX49 to pre-miR-145. A) RIP assays showing enrichment of pre-miR-145 with Flag-BYSL or HA-DDX49 alone, or with co-expression (CoExp) of both proteins in TPC-1 cells. IgG served as a negative control. Data represent mean ± SD, n=3. Statistical significance was determined by one-way ANOVA with Tukey's post hoc test. *p<0.05, **p<0.01; B) RIP analysis following siRNA-mediated silencing of BYSL or DDX49. Pre-miR-145 enrichment was assessed in the presence or absence of Flag-BYSL and/or HA-DDX49 in TPC-1 cells. IgG served as a negative control. Data represent mean ± SD, n=3. *p<0.05, **p<0.01; C) Western blot analysis of BYSL and DDX49 protein levels under the indicated conditions, with GAPDH as a loading control. Densitometric quantification normalized to GAPDH is shown on the right. D) Specificity analysis: RIP assays showing BYSL and DDX49 binding specificity to different pre-miRNAs in 8505C cells. Data represent mean ± SD, n=3. **p<0.01 vs. IgG control.

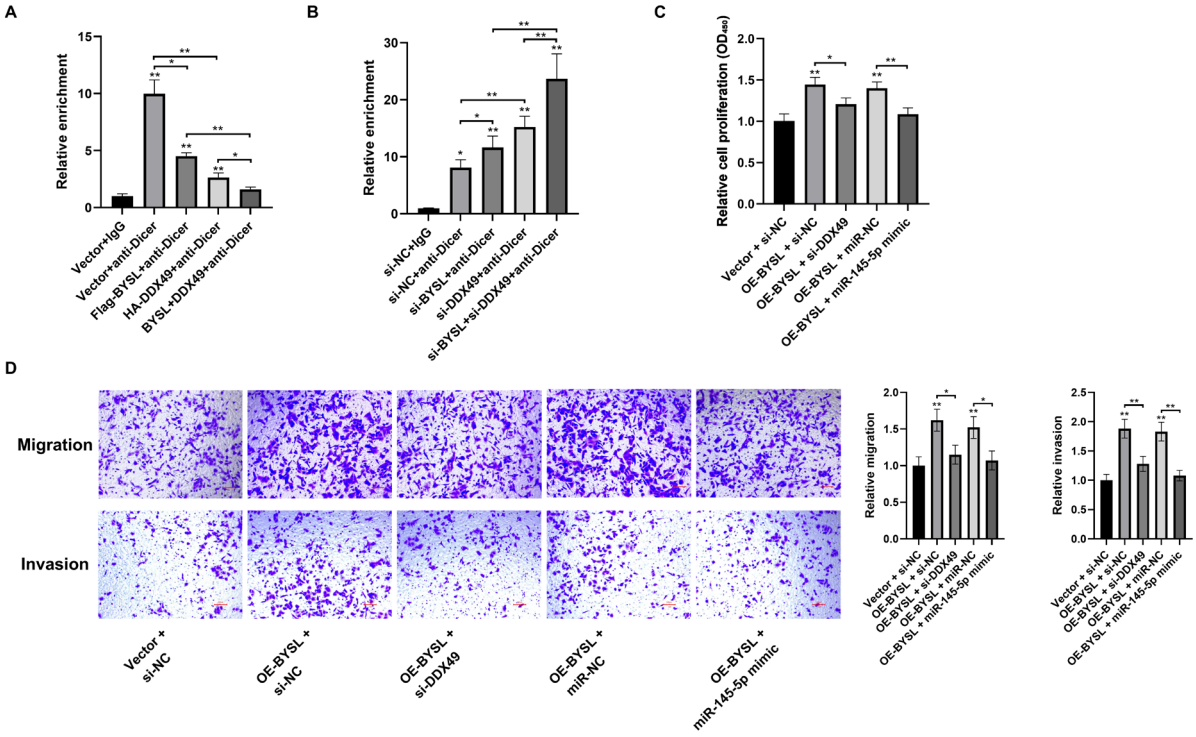

Figure 6. Effects of the BYSL-DDX49 complex on DICER-mediated pre-miR-145 processing and tumor cell phenotypes. A) RNA immunoprecipitation (RIP) assays showing enrichment of pre-miR-145 associated with DICER under conditions of overexpression of BYSL (Flag-BYSL), DDX49 (HA-DDX49), or both (BYSL+DDX49) in thyroid cancer cells. IgG was used as a negative control. Data represent mean ± SD, n=3. *p<0.05, **p<0.01 (one-way ANOVA with Tukey's post hoc test); B) RIP analysis of pre-miR-145 enrichment with DICER following silencing of BYSL (si-BYSL), DDX49 (si-DDX49), or both, compared to negative control (si-NC). Data represent mean ± SD, n=3. *p<0.05, **p<0.01; C) Cell proliferation assay (CCK-8) in thyroid cancer cells with BYSL overexpression (OE-BYSL) in combination with DDX49 silencing (si-DDX49) or miR-145-5p mimic transfection, compared to controls. Data represent mean ± SD, n=3. *p<0.05, **p<0.01; D) Representative images and quantification of Transwell migration (top) and invasion (bottom) assays in thyroid cancer cells under the indicated treatments. Data represent mean ± SD, n=3. *p<0.05, **p<0.01; Abbreviations: RIP-RNA immunoprecipitation; OE-BYSL-BYSL overexpression; si-NC-negative control siRNA; si-BYSL-BYSL knockdown; si-DDX49-DDX49 knockdown.

control levels. These findings indicate that the tumor-suppressive properties of BYSL/DDX49 silencing are predominantly mediated through miR-145-5p upregulation.

Discussion

In this investigation, we identify BYSL as a novel oncogenic mediator in thyroid malignancies, demonstrating that it constitutes a functional complex with DDX49 to modulate tumor progression. We demonstrate that BYSL exhibits substantial upregulation in thyroid malignancy specimens and cellular models, and that its enhanced abundance correlates with adverse clinical prognosis. Mechanistically, BYSL and DDX49 interact to establish a protein complex that regulates RNA metabolism, including miR-145-5p maturation control, consequently facilitating malignant characteristics. Importantly, PTC models confirmed the functional importance and clinical significance of this regulatory network, emphasizing its potential as a therapeutic target.

Our characterization of BYSL as an oncogenic mediator in thyroid malignancies is concordant with previous investigations in other neoplasms, such as hepatocellular carcinoma and glioblastoma, where BYSL upregulation is linked with tumor advancement and adverse prognosis [9, 11, 30]. Notably, in thyroid malignancies, BYSL expression was associated with OS outcomes but did not correlate with conventional clinicopathological variables such as tumor dimensions or lymph node involvement, indicating a broader function in tumor biology beyond cellular proliferation. Functional investigations demonstrated that BYSL silencing impairs proliferative capacity, motility, and invasiveness, while promoting apoptosis *in vitro* and *in vivo*, establishing comprehensive evidence for its oncogenic activity in thyroid malignancies.

A major advance of this work is the discovery of a direct interaction between BYSL and DDX49, which expands our understanding of BYSL's role in cancer biology. Both co-IP and immunofluorescence co-localization assays confirmed that this interaction occurs in both the nucleolus and cytoplasm, which aligns with the known subcellular localization of these proteins [7, 17, 31]. While our co-IP data establish interaction, they were not designed to quantify

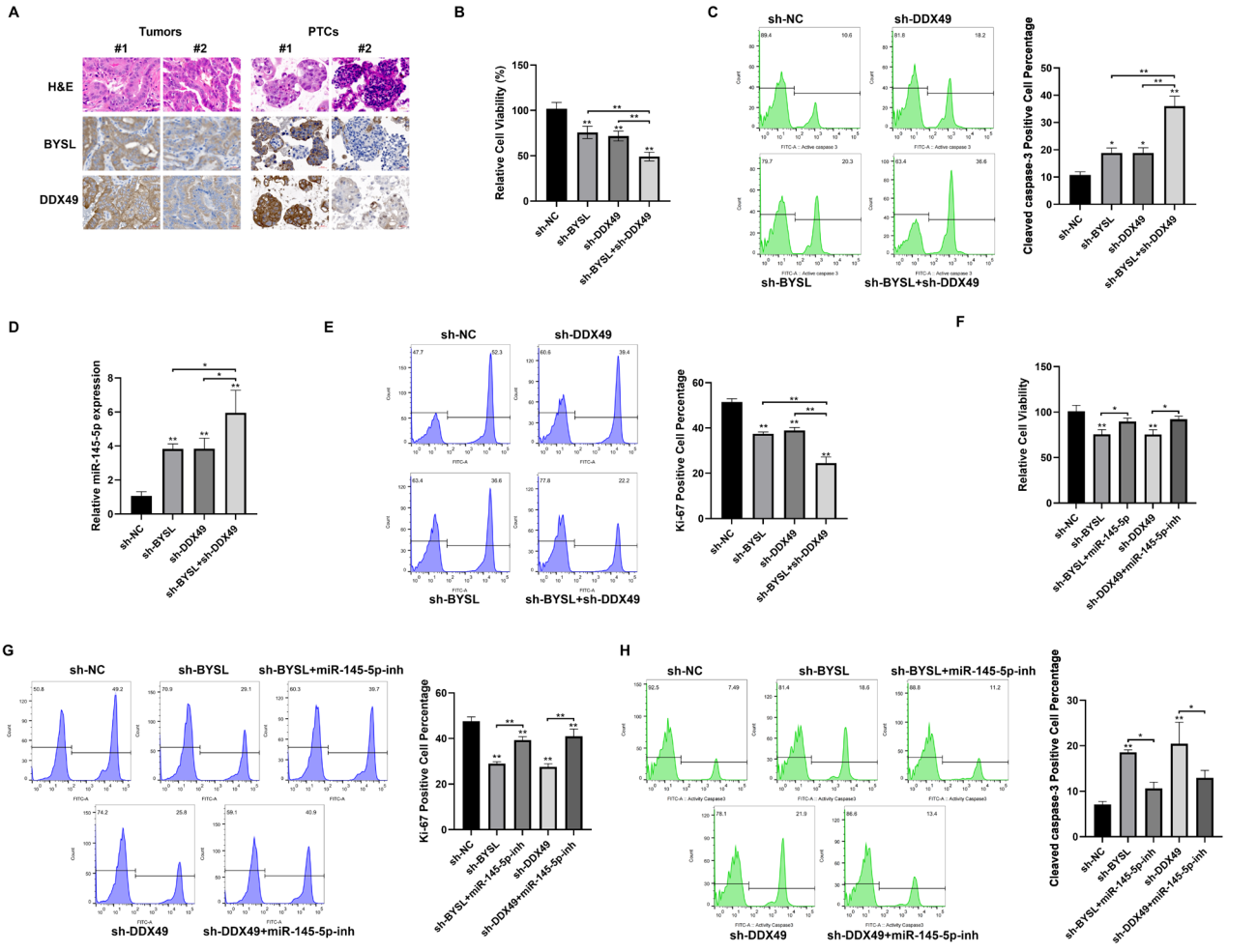

Figure 7. Functional and mechanistic analysis of BYSL-DDX49-miR-145-5p axis using patient-derived tumor-like cell clusters (PTCs). A) Immunohistochemical staining of BYSL and DDX49 in PTC models derived from primary thyroid cancer specimens; B) Cell viability of PTCs assessed after shRNA-mediated silencing of BYSL (sh-BYSL), DDX49 (sh-DDX49), or both (sh-BYSL+sh-DDX49), compared to negative control (sh-NC). Data represent mean ± SD, n=3. *p<0.05, **p<0.01; C) Flow-cytometric quantification of cleaved caspase-3-positive cells in the indicated groups; D) Relative expression of miR-145-5p in PTCs after the indicated treatments, measured by qRT-PCR; E) Flow-cytometric quantification of Ki-67-positive cells; F) Cell viability of PTCs after BYSL or DDX49 silencing with or without co-treatment with miR-145-5p inhibitor, measured by ATP activity assay; G) Percentage of Ki-67-positive cells after BYSL or DDX49 knockdown with or without the miR-145-5p inhibitor; H) Percentage of cleaved caspase-3-positive cells after BYSL or DDX49 knockdown with or without the miR-145-5p inhibitor; Abbreviations: sh-NC-negative-control shRNA; sh-BYSL-BYSL knockdown; sh-DDX49-DDX49 knockdown; miR-145-5p-inh-miR-145-5p inhibitor.

complex occupancy. Future work will assess complex stoichiometry by sequential immunoprecipitation or orthogonal biophysical approaches. The spatial distribution suggests that the BYSL-DDX49 complex may influence multiple aspects of RNA metabolism, from nuclear RNA processing to cytoplasmic RNA maturation. Furthermore, functional experiments demonstrated that DDX49 knockdown partly reverses the oncogenic phenotypes induced by BYSL overexpression, supporting a cooperative interaction essential for sustaining tumor cell malignancy.

At the mechanistic level, we uncovered a non-canonical mode of microRNA processing regulation, wherein the BYSL-DDX49 complex competitively binds to pre-miR-145, thereby interfering with DICER-mediated processing and suppressing the maturation of tumor-suppressive miR-145-5p. This mechanism is distinct from classic regulatory paradigms, which often involve direct modulation of core processing enzymes [32]. Our RIP data indicate that DDX49 is principally responsible for RNA recognition, while BYSL enhances the stability of this interaction. This cooperative binding adds to the expanding repertoire of post-transcriptional regulatory strategies in cancer.

The characterization of miR-145-5p as a downstream mediator of the BYSL-DDX49 axis is concordant with its well-documented tumor-suppressive function in thyroid malignancies [27–29]. Restoration of miR-145-5p partially

abrogated the oncogenic effects of BYSL overexpression, emphasizing the biological relevance of this regulatory network. It is important to note, however, that while our study focused on miR-145-5p due to its significant inverse correlation with BYSL and DDX49, it is likely that the BYSL-DDX49 complex also regulates additional RNA targets relevant to tumorigenesis.

The use of patient-derived tumor-like cell clusters in this study provides strong translational support for our findings. These models better recapitulate the heterogeneity and microenvironmental context of human tumors than conventional cell lines [26, 33–35]. miR-145-5p restoration partially counteracted the oncogenic properties of BYSL upregulation, underscoring the biological significance of this regulatory pathway. Nevertheless, it merits consideration that while our investigation concentrated on miR-145-5p due to its substantial inverse association with BYSL and DDX49, it is probable that the BYSL-DDX49 complex additionally modulates supplementary RNA substrates pertinent to tumorigenesis.

Our findings have important clinical implications. BYSL may serve as a prognostic biomarker to identify high-risk thyroid cancer patients who could benefit from more aggressive treatment strategies. Additionally, the BYSL-DDX49 complex represents a novel therapeutic target, with potential intervention strategies including direct inhibition of protein expression, disruption of protein-protein interaction, or restoration of tumor-suppressive RNAs. The observed synergistic effect of dual targeting further supports the concept of combinatorial therapeutic approaches.

Multiple constraints of this investigation merit recognition. Initially, although we demonstrated a correlation between BYSL expression and OS outcomes, validation in larger, independent patient populations is required to confirm its prognostic significance. Additionally, while our mechanistic investigations concentrated on miR-145-5p, the BYSL-DDX49 complex may modulate a broader array of RNA substrates, necessitating additional investigation. Furthermore, although PTCs provide a more physiologically representative model, they do not completely recapitulate the intricacies of the *in vivo* tumor microenvironmental context.

Future investigations should endeavor to comprehensively elucidate the BYSL-DDX49 interactome and transcriptome-wide RNA substrates, as well as investigate the involvement of this regulatory network across distinct thyroid malignancy subtypes. The development of small-molecule antagonists targeting the BYSL-DDX49 interaction represents a promising therapeutic strategy that warrants further investigation.

In summary, this study identifies a novel oncogenic regulatory axis in thyroid cancer, in which BYSL and DDX49 form a functional complex that modulates RNA metabolism and suppresses the maturation of tumor-suppressive miR-145-5p. This mechanism promotes thyroid cancer progression and represents a potential therapeutic vulnerability, advancing our understanding of the molecular pathogenesis of thyroid cancer and providing a rationale for the development of innovative diagnostic and therapeutic strategies.

Supplementary information is available in the online version of the paper.

Acknowledgments: This study was funded by the Scientific and Technological Innovation Project of China Academy of Chinese Medical Sciences (CI2021A01903, CI2021A01611).

References

[1] BOUCAI L, ZAFEREO M, CABANILLAS ME. Thyroid Cancer: A Review. JAMA 2024; 331: 425–435. https://doi.org/10.1001/jama.2023.26348

[2] CHEN DW, LANG B, MCLEOD D, NEWBOLD K, HAYMART MR. Thyroid cancer. Lancet 2023; 401: 1531–1544. https://doi.org/10.1016/S0140-6736(23)00020-X

[3] ZHANG J, XU S. High aggressiveness of papillary thyroid cancer: from clinical evidence to regulatory cellular networks. Cell Death Discov 2024; 10: 378. https://doi.org/10.1038/s41420-024-02157-2

[4] BOUDINA M, ZISIMOPOULOU E, XIROU P, CHRISOULIDOU A. Aggressive Types of Malignant Thyroid Neoplasms. J Clin Med 2024; 13: 6119. https://doi.org/10.3390/jcm13206119

[5] GUO M, SUN Y, WEI Y, XU J, ZHANG C. Advances in targeted therapy and biomarker research in thyroid cancer. Front Endocrinol (Lausanne) 2024; 15: 1372553. https://doi.org/10.3389/fendo.2024.1372553

[6] GIL-BERNABé S, GARCíA-DELAFUENTE L, GARCíA-ROSTáN G. The Revolution of Targeted Therapies in Thyroid Cancer Treatment: Present and Future Promising Anti-Cancer Drugs. Int J Mol Sci 2025; 26: 3663. https://doi.org/10.3390/ijms26083663

[7] AOKI R, SUZUKI N, PARIA BC, SUGIHARA K, AKAMA TO et al. The Bysl gene product, bystin, is essential for survival of mouse embryos. FEBS Lett 2006; 580: 6062–6068. https://doi.org/10.1016/j.febslet.2006.09.072

[8] FUKUDA MN, MIYOSHI M, NADANO D. The role of bystin in embryo implantation and in ribosomal biogenesis. Cell Mol Life Sci 2008; 65: 92–99. https://doi.org/10.1007/s00018-007-7302-9

[9] GAO S, SHA Z, ZHOU J, WU Y, SONG Y et al. BYSL contributes to tumor growth by cooperating with the mTORC2 complex in gliomas. Cancer Biol Med 2021; 18: 88–104. https://doi.org/10.20892/j.issn.2095-3941.2020.0096

[10] ADACHI K, SOETA-SANEYOSHI C, SAGARA H, IWAKURA Y. Crucial role of Bysl in mammalian preimplantation development as an integral factor for 40S ribosome biogenesis. Mol Cell Biol 2007; 27: 2202–2214. https://doi.org/10.1128/MCB.01908-06

[11] SHA Z, ZHOU J, WU Y, ZHANG T, LI C et al. BYSL Promotes Glioblastoma Cell Migration, Invasion, and Mesenchymal Transition Through the GSK-3β/β-Catenin Signaling Pathway. Front Oncol 2020; 10: 565225. https://doi.org/10.3389/fonc.2020.565225

[12] JIA Y, JIA R, CHEN Y, LIN X, AISHAN N et al. The role of RNA binding proteins in cancer biology: A focus on FMRP. Genes Dis 2025; 12: 101493. https://doi.org/10.1016/j.gendis.2024.101493

[13] LIU WW, ZHENG SQ, LI T, FEI YF, WANG C et al. RNA modifications in cellular metabolism: implications for metabolism-targeted therapy and immunotherapy. Signal Transduct Target Ther 2024; 9: 70. https://doi.org/10.1038/s41392-024-01777-5

[14] MA X, LU T, YANG Y, QIN D, TANG Z et al. DEAD-box helicase family proteins: emerging targets in digestive system cancers and advances in targeted drug development. J Transl Med 2024; 22: 1120. https://doi.org/10.1186/s12967-024-05930-0

[15] SILVERMAN E, EDWALDS-GILBERT G, LIN RJ. DExD/H-box proteins and their partners: helping RNA helicases unwind. Gene 2003; 312: 1–16. https://doi.org/10.1016/s0378-1119(03)00626-7

[16] MONTPETIT B, SEELIGER MA, WEIS K. Analysis of DEAD-box proteins in mRNA export. Methods Enzymol 2012; 511: 239–254. https://doi.org/10.1016/B978-0-12-396546-2.00011-5

[17] AWASTHI S, VERMA M, MAHESH A, K KHAN MI, GOVINDARAJU G et al. DDX49 is an RNA helicase that affects translation by regulating mRNA export and the levels of pre-ribosomal RNA. Nucleic Acids Res 2018; 46: 6304–6317. https://doi.org/10.1093/nar/gky231

[18] WANG Y, YANG L, LI X, YANG Q, MA R et al. Expression of DDX49 in breast cancer and its mechanism regulating the proliferation and metastasis of breast cancer cells. Growth Factors 2025; 43: 45–55. https://doi.org/10.1080/08977194.2025.2484007

[19] TAO J, GE Q, MENG J, LIANG C, HAO Z et al. Overexpression of DDX49 in prostate cancer is associated with poor prognosis. BMC Urol 2023; 23: 66. https://doi.org/10.1186/s12894-023-01251-4

[20] CHEN Y, MA Q, SUN N. DDX49 Promotes Proliferation and Metastasis of Cervical Cancer by Regulation of AKT and Wnt/β-Catenin Signalings. Ann Clin Lab Sci 2023; 53: 271–277.

[21] GALLARDO-DODD CJ, KUTTER C. The regulatory landscape of interacting RNA and protein pools in cellular homeostasis and cancer. Hum Genomics 2024; 18: 109. https://doi.org/10.1186/s40246-024-00678-6

[22] SLOAN KE, BOHNSACK MT. Unravelling the Mechanisms of RNA Helicase Regulation. Trends Biochem Sci 2018; 43: 237–250. https://doi.org/10.1016/j.tibs.2018.02.001

[23] LI J, LIU S, ZHOU H, QU L, YANG J. starBase v2.0: decoding miRNA-ceRNA, miRNA-ncRNA and protein-RNA interaction networks from large-scale CLIP-Seq data. Nucleic Acids Res 2014; 42: D92–97. https://doi.org/10.1093/nar/gkt1248

[24] KANG YJ, PAN L, LIU Y, RONG Z, LIU J et al. GEPIA3: Enhanced drug sensitivity and interaction network analysis for cancer research. Nucleic Acids Res 2025; 53: W283–W290. https://doi.org/10.1093/nar/gkaf423

[25] SZKLARCZYK D, KIRSCH R, KOUTROULI M, NASTOU K, MEHRYARY F et al. The STRING database in 2023: protein-protein association networks and functional enrichment analyses for any sequenced genome of interest. Nucleic Acids Res 2023; 51: D638–D646. https://doi.org/10.1093/nar/gkac1000

[26] YIN S, XI R, WU A, WANG S, LI Y et al. Patient-derived tumor-like cell clusters for drug testing in cancer therapy. Sci Transl Med 2020; 12: eaaz1723 [pii]. https://doi.org/10.1126/scitranslmed.aaz1723

[27] TORAIH EA, FAWZY MS, NING B, ZERFAOUI M, ERRAMI Y et al. A miRNA-Based Prognostic Model to Trace Thyroid Cancer Recurrence. Cancers (Basel) 2022; 14: 4128. https://doi.org/10.3390/cancers14174128

[28] ZHANG W, JI W, LI T, LIU T, ZHAO X. MiR-145 functions as a tumor suppressor in Papillary Thyroid Cancer by inhibiting RAB5C. Int J Med Sci 2020; 17: 1992–2001. https://doi.org/10.7150/ijms.44723

[29] BOUFRAQECH M, ZHANG L, JAIN M, PATEL D, ELLIS R et al. miR-145 suppresses thyroid cancer growth and metastasis and targets AKT3. Endocr Relat Cancer 2014; 21: 517–531. https://doi.org/10.1530/ERC-14-0077

[30] ZHANG J, TANG H, JIANG X, HUANG N, WEI Q. Hypoxia-Induced miR-378a-3p Inhibits Osteosarcoma Invasion and Epithelial-to-Mesenchymal Transition via BYSL Regulation. Front Genet 2021; 12: 804952. https://doi.org/10.3389/fgene.2021.804952

[31] MIYOSHI M, OKAJIMA T, MATSUDA T, FUKUDA MN, NADANO D. Bystin in human cancer cells: intracellular localization and function in ribosome biogenesis. Biochem J 2007; 404: 373–381. https://doi.org/10.1042/BJ20061597

[32] KOMATSU S, KITAI H, SUZUKI HI. Network Regulation of microRNA Biogenesis and Target Interaction. Cells 2023; 12: 306. https://doi.org/10.3390/cells12020306

[33] LIN F, YIN S, ZHANG Z, YU Y, FANG H et al. Multimodal targeting chimeras enable integrated immunotherapy leveraging tumor-immune microenvironment. Cell 2024; 187: 7470–7491.e32. https://doi.org/10.1016/j.cell.2024.10.016

[34] XU S, YIN SY, BIE ZX, LI YM, QI J et al. Personalized drug screening of patient-derived tumor-like cell clusters based on specimens obtained from percutaneous transthoracic needle biopsy in patients with lung malignancy: a real-world study. BMC Cancer 2025; 25: 649. https://doi.org/10.1186/s12885-025-14069-0

[35] GAO T, HE X, WANG J, LIU J, HU X et al. Self-assembled patient-derived tumor-like cell clusters for personalized drug testing in diverse sarcomas. Cell Rep Med 2025; 6: 101990. https://doi.org/10.1016/j.xcrm.2025.101990

https://doi.org/10.4149/neo_2025_250729N326

Bystin-like protein forms a functional complex with DDX49 to enhance thyroid cancer progression

Yue WANG[1,#], Xiaoxiao XING[1,#], Dongpo ZHANG[1,#], Tao SUN[2,#], Yuren ZHANG[3], Jun LI[1], Daixiang LIAO[1,*], Junyi LI[1,*]

Supplementary Information

Supplementary Table S1. shRNA sequences used in this study.

Gene	shRNA ID	Sense target (5'–3')	Loop	Antisense (5'–3')	Full top oligo (5'–3')
BYSL	sh-BYSL	CGAAATCAGGC-GTGAGC	TTCAAGAGA	GCTCACGCCTGATTCG	CACCGCGAAATCAGGCGTGAGCTTCAAGAGA-GCTCACGCCTGATTCGTTTTTTG
DDX49	sh-DDX49	CACTTTTAGTATA-AAGAAGA	TTCAAGAGA	TCTTCTTTATACTA-AAAGTG	CACCGCACTTTTAGTATAAAGAAGATTCAAGAGA-TCTTCTTTATACTAAAAGTGTTTTTTG
Non-targeting	sh-NC	TTCTCCGAACGT-GTCACGT	TTCAAGAGA	ACGTGACACGTTCG-GAGAA	CACCGTTCTCCGAACGTGTCACGTTTCAAGAGA-ACGTGACACGTTCGGAGAATTTTTTG

Supplementary Table S2. Primer sequences used in RT-PCR.

Gene name	Primer sequence (form 5' to 3')	Reference Sequence
DDX49	F: AGACAGCAGCGTTTGTCCTT	NM_019070.5
	R: TGCTCTGCGATCTGGTAGG	
DDX49 3'UTR	F: CCAGTCCTTGACTCGTCCAT	NM_019070.5
	R: ACCTCCCGGTCATGTTCTTT	
GAPDH	F: GGTGGTCTCCTCTGACTTCAACA	NM_002046.7
	R: GTGGTCGTTGAGGGCAATG	
PolyT adapter	GCGAGCACAGAATTAATACGACTCACTATAGGTTTTTTTTTTTTVN	
Universal Adaptor primer	GCGAGCACAGAATTAATACGAC	
RNU6B	F: CTCGCTTCGGCAGCACA	NR_004394.1
	R: GCGAGCACAGAATTAATACGAC	
hsa-miR-145-5p	F: GTCCAGTTTTCCCAGGAATC	NR_029686.1
	R: GCGAGCACAGAATTAATACGAC	
pre-miR-145	F: TCACGGTCCAGTTTTCCCAGGAATCCCTTAGATGCT	NR_029686.1
	R: GGTCCAGTTTTTTTTTTTTTTTAACCA	
pre-miR-21	F: CTTATCAGACTGATGTTGACTGTTGAATCTCATGGCAACACCAG	NR_029493.1
	R: CCAGTTTTTTTTTTTTTTTGTCAGAC	
pre-let-7a	F: TAGTAGGTTGTATAGTTTTAGGGTCACACCCACCACTGGGAGA	NR_029476.1
	R: GTCCAGTTTTTTTTTTTTTTTAGGAAAG	
pre-miR-200c	F: ACCCAGCAGTGTTTGGGTGCGGTTGGGAGTCTCTAATACTGCCGGGTAATGATG	NR_029779.1
	R: GGTCCAGTTTTTTTTTTTTTTTCCT	

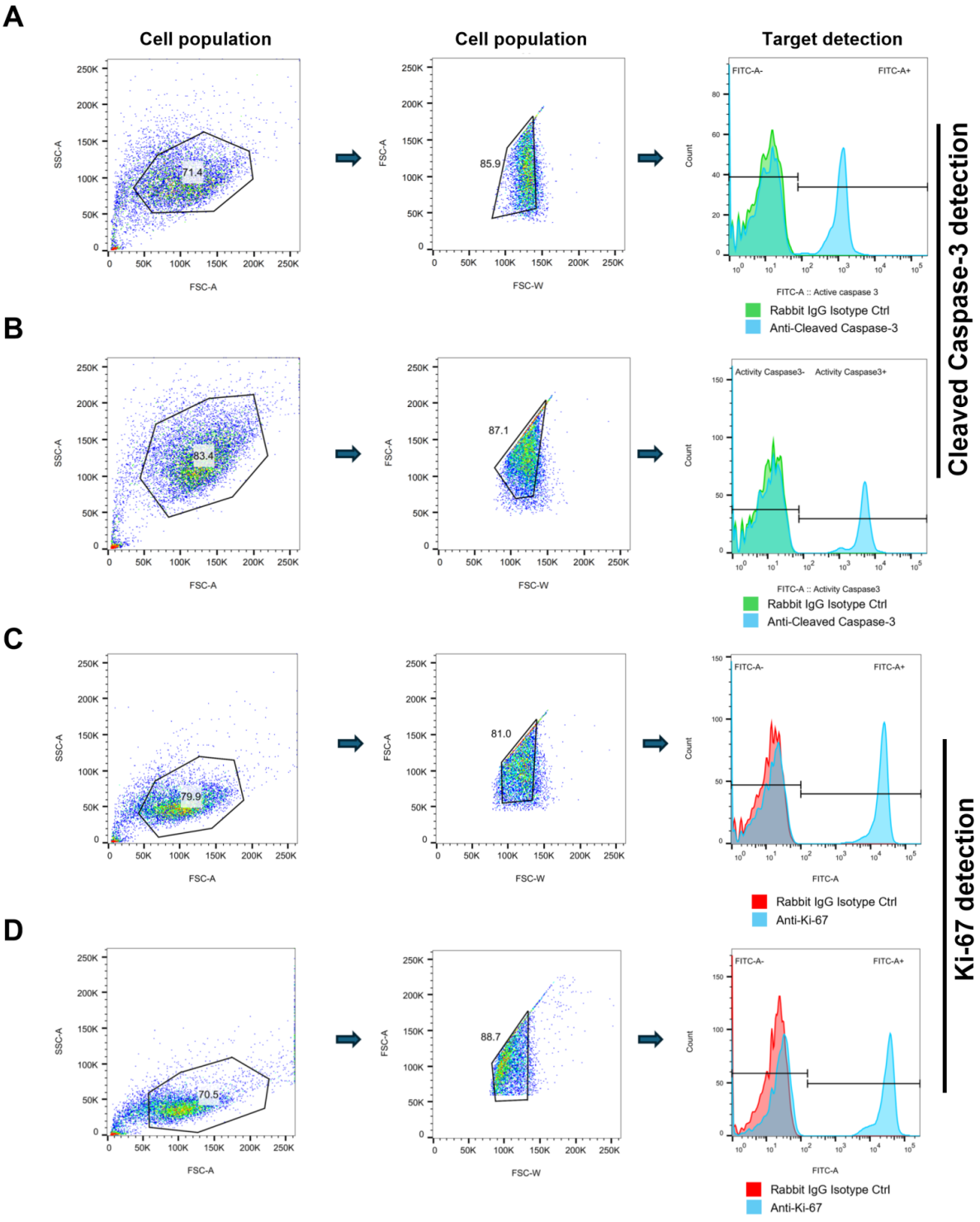

Supplementary Figure S1. Gating strategy and batch-matched, isotype-anchored thresholding for intracellular cleaved caspase-3 and Ki-67.
Debris was excluded using an FSC-A vs. SSC-A gate, followed by singlet selection on FSC-A versus FSC-W. Within the singlet population, FITC-A histograms of the matched rabbit IgG isotype and the antibody-stained sample (acquired with identical PMT/compensation settings) are shown side-by-side. The positivity threshold is positioned at the 99th percentile of the isotype control (≤ 1% isotype-positive events) and then applied unchanged to the corresponding stained sample within the same batch. Percentages in the scatter plots denote the fraction of events retained at each gate; histogram-based positive rates are calculated within singlets. Axes: x, fluorescence intensity (FITC-A, logarithmic); y, counts. All histograms use identical axis scaling. Isotype panels used for gate determination correspond to Figure 7 as follows: S1A → Figure 7C (cleaved caspase-3), S1B → Figure 7H (cleaved caspase-3), S1C → Fig.ure 7E (Ki-67), and S1D → Figure 7G (Ki-67).

Supplementary Table S3. Composition and reagent information of the serum-free PTC growth medium used in this study (adapted from Yin et al., Sci Transl Med 2020).

Component/Additive	Supplier	Catalog No.	Final concentration	Notes
Advanced DMEM (base)	Gibco	12491-015	-	Base medium
HEPES (1 M)	Gibco	15630-080	1 mM	Buffer
GlutaMAX (100×)	Gibco	35050-061	1×	L-glutamine substitute
Penicillin–Streptomycin (100×)	Gibco	15140-122	100 U/ml+100 μg/ml	Antibiotics
B27 (50×)	Thermo Fisher	17504-044	1×	Serum-free supplement
Non-essential amino acids (100×)	Gibco	11140-050	1×	NEAA
EGF	PeproTech	AF-100-15	40 ng/ml	Growth factor
FGF-basic (bFGF)	PeproTech	AF-100-18B	20 ng/ml	Growth factor
R-spondin-1	Novoprotein	CX83	500 ng/ml	Wnt pathway agonist
Noggin	Novoprotein	CB89	100 ng/ml	BMP inhibitor
Nicotinamide	Sigma-Aldrich	N0636	10 mM	Vitamin B3 derivative
A83-01	Tocris	2939	0.5 μM	TGF-β receptor inhibitor
SB202190	Sigma-Aldrich	S7067	10 μM	p38 MAPK inhibitor
Y-27632-07	GeneX Health	GX-C-07	10 μM	ROCK inhibitor
N-acetyl-L-cysteine (NAC)	Sigma-Aldrich	A9165	1 mM	ROS scavenger
HGF	PeproTech	100-39	30 ng/ml	Growth factor
MSP	R&D Systems	352-MS	5 ng/ml	Growth factor
Prostaglandin E2 (PGE2)	Tocris	2296	10 nM	Prostaglandin